Version of Record: https://www.sciencedirect.com/science/article/pii/S0013468622010799
Manuscript_6c29958e7ec159671113b0acf3460c4d

Failure Analysis of Solid Oxide Fuel Cells Nickel-Yttria Stabilized Zirconia Anode under Siloxane Contamination

Jiashen Tian[a], Ryan J. Milcarek[a*]
[a.] School for Engineering of Matter, Transport and Energy, Arizona State University
501 E. Tyler Mall, Tempe, AZ 85287, USA

Abstract:

In this study, the failure process of the solid oxide fuel cell (SOFC) Ni-yttria-stabilized zirconia (YSZ) anode is investigated with D4 siloxane (octamethylcyclotetrasiloxane) contamination. In order to evaluate the influence of the electrochemical reaction on the siloxane deposition process, the SOFC experiments were operated at open circuit voltage (OCV) and 50 mA cm^{-2} conditions at 800 °C. During the failure process, electrochemical, morphology and exhaust gas component analysis testing are conducted at the critical points. An equivalent circuit model and corresponding microstructure parameter calculations for separated physicochemical processes were utilized for the quantitative analysis of the failure process. The results confirm the siloxane chemical adsorption deposition mechanism proposed in previous work. As a result, the failure of the anode was attributed to the gas diffusion blockage by dense silicon dioxide layer formation. The anode failure process with siloxane contamination is faster when the anode is operated under polarization.

Keywords: Solid oxide fuel cell (SOFC); Siloxane; Failure; Degradation; Equivalent circuit Model (ECM); Anode microstructure quantification.

*Corresponding author. E-mail address: Ryan.Milcarek@asu.edu (R. Milcarek).

1. Introduction

For the solid oxide fuel cells (SOFCs') anode, several degradation mechanisms including intrinsic degradation, Ni-agglomeration, densification/sintering, sulfur poisoning, carbon and silicon deposition all contribute to the overall cell performance loss. Generally those mechanisms can be categorized into two types [1]. One type of degradation results in gradual performance decay such as intrinsic degradation, Ni-agglomeration and densification/sintering [2,3]. For external sources of contamination, mechanisms like sulfur poisoning or carbon and siloxane deposition, there is also the gradual/soft degradation period initially which is similar to the gradual degradation mechanism. However, an obviously even sudden failure occurs after the gradual decay over a relatively short period of time.

External sources of contamination like sulfur and carbon have been explored for many years [4–15]. For anode poisoning by hydrogen sulfide, Li et al. reported that the sudden failure due to H_2S poisoning mainly happened after a 5 minutes stable period at 0.2% contamination [16]. During exposure to ppm(v) level concentration of H_2S there are hundreds of hours of soft degradation period initially and then obvious failure happened within hours shown in the research from Rasmussen et al. [9]. Compared with H_2S, the anode degradation mechanism due to carbon deposition also exhibits separated soft and rapid degradation periods but comparably longer failure time. In the study from Koh et al. [17], with dry methane as the fuel, the SOFC experienced around 250 hours of relative stable/slow degradation and then a significant performance loss. Similarly, Dhir et al. [18] reported the failure event happened after nearly 4 hours of stable operation under 0.625 A cm^{-2} current density with pure methane fuel.

Silicon based compounds, such as siloxanes which are detected in biogas or biomethane, are detrimental to SOFC applications [19–21]. Similar to sulfur and carbon, the SOFC anode failure process for silicon from siloxane contamination should also follow a similar trend with other external contamination sources. However, there are only limited reports about SOFC failure process due to siloxane contamination. Madi et al. reported over 800 hours single cell and over 100 hours of stack gradual degradation with ppm(v) level D4 siloxanes contamination [22,23]. Papurello et al. demonstrated 50 hours slow performance degradation process with ppb level of D4 siloxanes [24]. 100 hours of soft performance degradation of SOFCs has been reported by Kikuchi et al. [5] with ppm(v) level D5 siloxanes contamination. Our previous research [25] with different fuels mixed with ppm(v) level D4 siloxanes also showed the gradual degradation process over 150 hours. To date, most of the degradation studies for siloxane contamination occurred in the slow degradation period. There is only one exception with Haga et al. [26] reporting the failure period of SOFCs with ppm(v) levels of D5 siloxanes at different temperatures within 40 hours. However, no detailed failure analysis has been reported.

For some gradual anode degradation mechanisms whose degradation extents are proportional to the stress level, such as temperature and current density, the performance loss can be predicted by accelerated lifetime tests with aggravated stress [1,2]. However, anode aging especially with extrinsic contamination sources is hard to predict due to separated stable and rapid degradation processes with significantly different degradation rates. For industrial applications the fuel quality criteria with tolerances to different impurities under the certain concentrations is applied empirically to confirm the cleanliness of fuel and prevent

short-term failure of cells [27]. However, reports on the tolerance concentration vary due to dependence on the type of cells and operation conditions [28]. The failure event (joint point between stable and fast degradation) is extremely important for degradation mechanism studies and degradation predictions related to external contamination sources. For hydrogen sulfide, an acceleration experiment suggests that the sulfur/sulfide composition, such as nickel sulfide, generated at the active layer of anode near anode/electrolyte interface causes the fast degradation and failure of SOFCs. No obvious sulfur deposition was found on the anode surface which indicates the diffusion layer of anode did not influence the sulfur poisoning significantly [16]. However, for siloxane contamination, the studies mainly focus on the slow degradation mechanism. Not enough failure mechanism analysis has been conducted.

From the previous siloxane deposition studies, a two-step mechanism was proposed by Haga et al. [29] to explain the silicon deposition and is shown in equation (1) and (2).

$$[(CH_3)_2SiO]_5(g) + 25H_2O(g) \rightarrow 5Si(OH)_4(g) + 10CO(g) + 30H_2(g) \quad (1)$$

$$Si(OH)_4(g) \rightarrow SiO_2(s) + 2H_2O(g) \quad (2)$$

The degradation of the SOFCs' anode is caused by the deposition of SiO_2 near the triple phase boundary (TPB) region. However, our previous study revealed that this two-step mechanism is not thermodynamically favorable [30]. Based on siloxane adsorption studies on Al_2O_3 filters as shown in equation (3), a similar process may also occur in SOFCs' Ni-YSZ anode and can be considered as an essential step for siloxane deposition [31,32]. Notably, the adsorption studies on Al_2O_3 report the formation of CH_4 instead of CO or H_2 as described in the two-step mechanism. However, due to the ppm(v) level contamination in previous

siloxane studies [25,30], analysis of the components of the reaction products can be extremely difficult to conduct.

$$\gamma\text{-}\ Al_2O_3\ \text{-}\ 8OH + \frac{7}{4}[SiO(CH_3)_2]_4 + 3H_2O \rightarrow\ \gamma\text{-}\ Al_2O_3\ \text{-}\ Si_7O_{18} + 14CH_4 \quad (3)$$

Morphology analysis from Madi et al. and our previous studies [22,25] also demonstrate that the silicon deposition mostly occurs near the surface of the anode which is far from the active layer of the Ni-YSZ anode. As a result, the failure of the anode can be attributed to either the invalidation of the TPB active region or the obstruction of the diffusion path.

In this study, an acceleration poisoning experiment is conducted with 0.5% D4 siloxane contamination to focus on the failure analysis of Ni-YSZ SOFC anode. To investigate the influence of electrochemical polarization on the failure of the SOFC due to siloxane contamination, the experiments were conducted at open circuit voltage (OCV) and 50 mA cm^{-2} current density conditions. Simultaneously, exhaust gas component analysis is implemented to verify the previously proposed mechanisms.

2. Experimental

2.1 Fuel cell and pellets fabrication

Electrolyte supported SOFCs were fabricated and utilized for the failure study. Most previous studies reported siloxane deposition occurred in the anode support layer (ASL) instead of the anode active layer (AAL) and utilized anode supported SOFCs [22,25]. With an anode supported SOFC and deposition occurring in the ASL it is difficult to investigate the influence of the electrochemical reactions on the siloxane deposition process. The thin anode layer in this study can reduce the impact of gas diffusion-related processes by

shortening the effective diffusion thickness. This is considered an important feature of this study as diffusion limitations and changes in the microstructure of the electrochemical active region have been cited previously as the cause of degradation from siloxane contamination [4,29]. The supported yttria-stabilized zirconia (YSZ, $(ZrO_2)_{0.92}(Y_2O_3)_{0.08}$, Fuelcellmaterials) electrolyte was prepared by die pressing and pre-sintered at 1100 °C for 4 hours. The wet power spray technique was utilized for the NiO+YSZ (60:40 w/w, Fuelcellmaterials) anode layer. The YSZ electrolyte and NiO-YSZ anode were co-sintered at 1400 °C for 4 hours. Strontium-doped lanthanum manganite (LSM, $(La_{0.80}Sr_{0.20})_{0.95}MnO_{3-x}$, Fuelcellmaterials) + YSZ (50:50 w/w) cathode was deposited on the electrolyte by wet powder spray. LSM-based cathode was chosen due to its low degradation rate compared to other cathodes in order to ensure the degradation observed in the fuel cell performance is primarily a result of siloxane contamination [33]. The cell was sintered at 1100 °C for 2 hours in air. After sintering, the thickness of electrolyte, cathode and anode are ~ 380 μm, ~ 20 μm and 17 μm, respectively.

For electrochemical characterization, electrochemical impedance spectroscopy (EIS) measurements were carried out with an Electrochemical Impedance Analyzer (Solartron Analytical Energylab XM) in a frequency range from 10^6 Hz to 0.1 Hz. All EIS measurements were conducted under open-circuit voltage (OCV) with 10 mV signal amplitude. The SOFCs' performance was also evaluated with polarization (j-V), power density and constant current operation (V-t curve) curves. The data was measured with four-probe technique and recorded by a digital SourceMeter (Keithley 2460) interfaced with LabView on the computer.

2.2 Testing setup

Fig. 1 shows the experimental setup utilized for the SOFCs' failure study with D4 siloxane contamination. The SOFCs were placed on the top of a quartz tube and sealed with silver paste. Silver ink was painted on the center of the cathode for current collection with 0.495 cm^2 active area. A pair of silver/steel wires were attached to the anode and cathode surface as probes for electrochemical measurements. For the anode fuel supply, H_2 (ultra high purity grade, Airgas) and N_2 (ultra high purity grade, Airgas) flow rates were controlled by Brooks Delta II smart mass flow controllers (MFCs) with LabView interface. To obtain the targeted siloxane concentration in the fuel, the liquid phase D4 siloxane was delivered to the fuel pipeline at a controlled flow rate by a syringe pump (PumpSystems Inc.). The D4 siloxane was vaporized with heat added from resistive heaters wrapped on the gas delivery pipe and carried to the SOFCs' anode by the H_2 and N_2 gases. To ensure the D4 siloxane maintained gas phase (D4 boiling point is about 176 °C) the T-type thermocouples (Omega) were mounted along the fuel delivery pipe for temperature inspection. The heat generation rate of the wrapped resistive heaters were adjusted individually to ensure the whole gas delivery pipeline maintained a stable temperature around 200 °C. The D4 siloxane flow rate was controlled at 0.1 standard cubic centimeters per minute (sccm). To avoid the potential reaction of D4 during delivery process and guarantee the concentration of D4 in the mixtures gases, the D4 siloxane is mixed close to the furnace. In this situation, the path of siloxane delivery can be shortened and potential loss of siloxane can be minimized. In order to have a good comparison with previous work [25,30,34], the H_2 flow rate was maintained constant at 7 sccm. The flow rate of N_2 gas was fixed at 12.9 sccm with the primarily purpose of diluting

the concentration of the D4 siloxane, similar to previous experiments [25]. For the SOFC accelerated degradation or failure studies, external contamination sources are usually mixed into the fuel with relatively large concentrations compared to the real application to highlight their influence. For H_2S, generally the contamination concentration can be found in ppm(v) level for the actual biogas applications, but to accelerate the degradation process and reaction in the SOFC anode, 0.2 to 10% were selected for some studies [16,35,36]. Similarly, the total flow rate of fuel gases (H_2, N_2, D4) was held at 20 sccm resulting in a D4 concentration of 0.5%. Gas composition analysis was also utilized to verify the concentration of D4 in the fuel. More details are discussed in the results section. The cathode was exposed to the air in the vertical furnace and the air supply was implemented through natural convection.

For all experiments in this study, the quartz tube reactor was fixed in the center of the vertical furnace. The furnace was heated at 5 °C per minute to an SOFC operating temperature of 800 °C. A K-type thermocouple inside the furnace near the SOFC was utilized to confirm the temperature. Before starting experiments, the YSZ-NiO SOFC anode was supplied with H_2 and N_2 at flow rates of 10 sccm individually for 4 hours to reduce the NiO to Ni. To avoid the impact of anode intrinsic degradation which typically occurs in the first few hours of operation, the SOFC was operated with the same flow rate of H_2 and N_2 for 24 hours. After stabilizing the performance of the SOFC, D4 siloxane was added to the mixture and the flow rates were adjusted to the values previously described. To have a better understanding of the failure process of the anode by siloxane contamination, three different special points were analyzed during the failure process. The first point (i.e., point 1) is right after the siloxane contamination started. This point is the baseline for the failure process and

also provides a chance to investigate the initial status of the degradation. The next and the most important point (i.e., point 2) is when the failure event begins because it may reveal the reason for the anode failure and detailed information about why the anode starts to degrade much faster after this point. The last point (i.e., point 3) is before the total failure of the SOFC. Comparison of this point with the second point at the failure initiation allows the rapid degradation and failure process to be analyzed. Electrochemical characterization tests were conducted with continuous V-t curves, and polarization and EIS results under both OCV and 50 mA cm^{-2} current density conditions were obtained at the three special points. For morphology and Photoelectron Spectroscopy (XPS) analysis, three samples obtained at each of the three different points are also necessary to represent the corresponding microstructure features. The exhaust gas composition obtained at each point was analyzed by a gas chromatograph (GC, Shimadzu FID-GC2014) with Restek Rtx-1 Columns (fused silica) column. In order to eliminate the disturbance that exhaust gas analysis could have on the electrochemical tests, they were conducted separately and both types of experiments were repeated several times with consistent results obtained each time. Considering that point 1 represents the initial status for the degradation process and should not have a significant difference in OCV and 50 mA cm^{-2} conditions, a single test for morphology, XPS and gas composition analysis was conducted instead of two to simplify the entire experimental process at this point. More details and description of these three special points can be found in the results section.

2.3 XPS characterization

The postmortem analysis of the anode surface was accomplished with a K-Alpha XPS (Krator Axis Supra +) with monochromatized Al K-Alpha X-rays source (1486.6eV). Survey spectra were recorded with an analyzer pass energy of 150 eV. After XPS characterization, the results were analyzed by the software CasaXPS version 2.3.24PR1.0.

2.4 Morphology Analysis

After the failure experiments, the samples obtained for morphology tests were crosscut and embedded in epoxy. The cross section of the samples were prepared by polishing with different grain size SiC papers, water-based diamond suspension and colloidal silica diamond suspension. More details about the sample preparation process can be found in our previous paper [25] which utilized similar techniques. The morphology of the SOFCs' cross section was investigated by a field emission scanning electron microscope (FESEM, JEOL JXA-8530F electron microprobe) equipped with wavelength-dispersive spectrometers (WDS). The electron beam was selected as 15 kV at 5×10^{-8} A for the SEM and WDS analysis.

3. Results and Discussion

3.1 Electrochemical characterization of the SOFC

For the SOFC D4 contamination failure experiments, nominally identical cells following same fabrication processes were utilized for the OCV and 50 mA cm^{-2} conditions. The cells' voltage changes as a function of time under D4 contamination as shown in **Fig. 2**. The OCV

of the SOFC is about 0.92V which has a good correspondence with the theoretical OCV calculation from Nernst equation based on diluted H_2 and O_2 as the fuel and oxidizer. Generally, the entire failure processes for the two experiments shared a similar pattern. As described in the introduction section, the SOFC failure process with siloxane contamination coincides appropriately with typical external contamination aging curves. The long and soft degradation period occurred at the beginning of the aging tests. The OCV declined from 0.92 V to 0.90 V during the first 95 minutes. For the SOFC operating at 50 mA cm^{-2}, the voltage decreased from 0.77 V to 0.73 V in 90 minutes. Subsequently, after the soft degradation period, the failure initiation events which have been marked as point 2 on the plot, appeared in both situations. Much higher degradation rates occurred after the initial failure point causing the sudden absolute failure of the SOFCs. Comparing the results from the OCV and 50 mA cm^{-2} experiments, the SOFC operating under polarization conditions had a faster failure process than when operating at OCV. This can be concluded from the fact that the 50 mA cm^{-2} experiment was about 5 minutes faster to reach the failure event point (point 2). Furthermore, from the initial failure event to complete failure, the 50 mA cm^{-2} experiment also has a higher degradation rate (0.04 V/min) compared to the OCV experiment (0.01 V/min). An interesting phenomenon can also be observed during the sudden failure process when a short, relatively lower degradation rate process occurs around point 3 labeled in the plot in both 50 mA cm^{-2} and OCV cases.

To have an accurate and precise evaluation of the entire SOFC failure process due to siloxane contamination, potential sources of error should be considered. The measured data in experiments was confirmed by uncertainty analysis. For this experimental study, the bias

(systematic) error and precision (random) error are considered. The bias error for the galvanostatic results of the entire failure process shown in **Fig. 2** is attributed to the resolution limit of the Solartron Analytical Energylab XM analyzer. In this situation, the resolution of the analyzer for the galvanostatic test can be obtained from the manual which is ±0.1% for the voltage measurement and 1 ms for time measurement. After calculation, the bias uncertainties from the analyzer can be ignored compared to the random error.

Repetition of the study can be utilized to calculate the precision error. As described before, in order to obtain samples for morphology and XPS analysis and to eliminate the disturbance that exhaust gas analysis causes, the galvanostatic tests for the failure process were repeated several times for each point. The voltage error bars of galvanostatic results for the failure experiment under OCV and 50 mA cm^{-2} at point 1 and point 2 were calculated and presented in **Fig. 2** because those points are utilized for the degradation rate comparison during the gradual decay phase. The random error for the time of point 2, where the SOFCs starts to decay faster, is also important for the failure process comparison. Comprehensively considering the uncertainty analysis results, the experimental data from point 1 and point 2 have acceptable accuracy for SOFC failure analysis. In order to have a more convincing conclusion, the galvanostatic test results still need to be reviewed with the other evidence such as morphology analysis results.

Besides the constant current density test, polarization curves were also obtained to characterize the degradation as shown in **Fig. 3**. In order to have a quantitative investigation of the degradation processes at certain essential points such as initial degradation, initial failure event, and the transition to sudden failure process, the measurements were

implemented after point 1, 2 and 3. The maximum power density of the electrolyte supported SOFCs were reported from ~ 100 mW cm^{-2} to 300 mW cm^{-2} normally [37,38]. For this work considering the thickness of the electrolyte and the anode, the low hydrogen concentration due to dilution in inert and low total flow rate, the maximum power density at point 1 was around 87 mW cm^{-2}. With a similar trend as the V-t curves in **Fig. 2**, the polarization curves in **Fig. 3** also demonstrate a relatively slow degradation process with less power density loss from point 1 to point 2 and larger power density decrease after the initial failure event (point 2) corresponding to the faster degradation process. For the OCV experiment, from point 1 to point 2, the maximum power density loss is about 8.86 mW cm^{-2}. In contrast, the SOFC maximum power density in the 50 mA cm^{-2} constant current density experiment decreased 41.44 mW cm^{-2} between point 1 and 2. This larger loss in power density is believed to be connected to the faster degradation rate after observing the initial failure event and is correlated with the higher voltage loss observed during the measurement process (**Fig. 2**).

In addition to the polarization curves, the EIS measurements were also utilized for the failure process analysis. From **Fig. 4**, obvious impedance increase can be noticed in both the OCV and 50 mA cm^{-2} current density experiments. With a similar trend to previous electrochemical characterization results, the total impedance increase for the 50 mA cm^{-2} constant current density experiment is much larger than the OCV experiment. In order to have a detailed quantitative analysis of the EIS results, an equivalent circuit model (ECM) was developed. Based on the SOFC with Ni-YSZ anode complex equivalent circuit models studies accomplished by Dierickx and Sonn et al. [39–42]., the ECM was built up with one resistor for ohmic resistance polarization; one Gerischer element attributing to cathode

process; one Warburg element representing the diffusion process and one two-channel transmission line model (TLM) for anode process. The TLM application in this study instead of the ordinary RQ element for the anode process can disclose more detailed information for the degradation of ionic transport and charge transfer in the failure process. Complex nonlinear least-squares (CNLS) fitting was utilized to analyze the impedance spectra with the commercial software Zview. For all ECM fitting results, χ^2 values were below 0.001. The TLM shown in the **Fig. 4** inserts is the distributed equivalent circuit element named "DX11-Bisquert 2" available in Zview. The model parameters for both OCV and 50 mA cm^{-2} show an excellent agreement with the other electrochemical results shown in **Fig. 2** to **Fig. 4**. The specific resistance values for the anode degradation are listed in **Table 1** from the ECM. The ohmic resistance, ionic transport resistance, charge transfer resistance and gas diffusion resistance corresponding to anode are denoted by R_{ohm}, r_{ion}, r_{ct}, and R_W, respectively.

Table 1
Equivalent circuit fitting results for anode degradation related polarization resistance.

Experimental Conditions	Time	R_{ohm} (Ω)	r_{ion} (Ω/μm)	r_{ct} (Ω μm)	R_W (Ω)
OCV	Point 1	2.98	0.042	1.23	1.69
	Point 2	3.08	0.049	1.96	1.83
	Point 3	3.08	0.055	2.64	6.33
50 mA cm^{-2}	Point 1	2.68	0.053	1.01	1.43
	Point 2	2.70	0.060	2.49	5.83
	Point 3	3.17	0.061	5.33	15.60

From **Table 1**, the ohmic resistance increase is observed in both the OCV and 50 mA cm^{-2} experiments. The larger ohmic resistance increasing for the SOFC operating at 50 mA cm^{-2} may be caused by more serious siloxane deposition which can jeopardize the Ni

conductive network through grain boundaries. For ionic transport resistance, only limited increase is observed in both experimental conditions. This phenomenon may be explained by the bulk conduction of oxygen ions through the dense YSZ grains. Hence, the surface deposition of siloxane may not have significant influence on this process [43]. The significant charge transfer resistance increase shown in **Table 1** demonstrates the failure of triple phase boundaries (TPB). Besides charge transfer resistance, the most significant resistance increase is from the diffusion polarization. Furthermore, diffusion polarization resistance increase follows the same trend of degradation shown in **Fig. 2** and **Fig. 3** in which a slow degradation process occurred between point 1 and point 2 and sudden degradation happened after point 2. Similarly, the SOFC in the 50 mA cm^{-2} experiment has much larger diffusion impedance increase compared to the OCV experiment. Based on the parameters from the ECM results, the degradation appears to be most correlated with the diffusion processes which may be primarily responsible for the failure process.

3.2 Morphology and XPS Analysis

Supplemental Fig. 1 shows the morphology analysis results at the initial status around point 1 as the reference for the comparison with point 2 and point 3. The left side with the dense layer is the interface between the YSZ electrolyte and Ni-YSZ anode and the anode surface is on the right. From the figure, some random weak silicon signals can be observed in the anode while a thin layer of carbon deposition can also be noticed at the surface of anode. This illustrates that siloxane deposition happened rapidly even at the beginning of the experiment and the carbon deposition may occur at the outer anode surface even before

significant silicon deposition. **Fig. 5** and **Fig. 6** depict the Si, C and O elements distribution over the entire anode cross section for OCV and 50 mA cm^{-2} experiments, respectively. For the OCV experiment in **Fig. 5**, compared with the initial status in **Supplemental Fig. 1**, obvious silicon deposition can be detected, especially with silicon accumulation on the anode surface after the failure event (point 2). After point 3, a layer of silicon has been established on the surface of the Ni-YSZ anode (**Fig. 5b**). A slight increase in carbon signal can also be perceived from WDS results at point 2 and point 3 following the silicon deposition.

In contrast to the results from the OCV experiment, the experiment under 50 mA cm^{-2} current illustrates a much quicker failure process (**Fig. 6**). Even after point 2, a thick layer of silicon deposition appeared on the surface of the anode. The high correlation of silicon and oxygen elements in the compact layer shown in morphology of the anode surface indicates silicon dioxide may be the composition of the dense layer. Comparing the elements distribution between point 2 and point 3, the surface deposition layer continued to grow until the absolute failure of the SOFC. More carbon deposition on the surface and inside the anode can also be observed compared to the OCV experiment. Comprehensively, the morphology results provide an excellent interpretation for the electrochemical results presented in **Fig. 2** to **Fig. 4**. The surface deposition layer formed after point 2 is interpreted as causing the sudden SOFC failure due to obstruction of the fuel diffusion path. The region with slightly lower degradation rate observed near point 3 on the V-t curve in **Fig. 2** may relate to the dense layer formation process. During the initial dense barrier layer formation phase, since the diffusion paths are not completely closed, the degradation continues at a comparatively

slow speed. However, when the entire surface is almost covered by the dense silicon dioxide, dramatic degradation occurs until complete failure.

To determine the composition of the siloxane deposition, XPS analysis has been conducted on the surface of the Ni-YSZ anode after point 1, point 2, point 3 and complete failure in OCV experiments, respectively. For the contamination element detection, inspired by previous studies [25,30,34] and also the SEM/WDS results in this study, silicon, carbon and oxygen elements were selected as the targets for the spectra. **Table 2** lists the results of XPS analysis of silicon, carbon and oxygen elements by atomic percentage. After point 1 in the OCV experiment, significant carbon deposition can be identified, and only limited silicon deposition can be found. This result is in good agreement with the morphology analysis results for point 1 presented in **Supplemental Fig. 1**. Combining the XPS and morphology results, it can be concluded that at the initial state of siloxane deposition on Ni-YSZ anode, carbon is deposited first. Throughout the failure process the percentage of carbon on the surface continuously decreases. After the initial failure event (point 2), a significant increase in silicon is noted compared with the results after point 1. Coincidently, the sudden performance degradation happened after this initial failure event. From point 2 to complete failure, the silicon element increased gradually. While the percentage of oxygen is also increasing following the silicon, eventually, the ratio of Si:O is near 1:2 after complete failure. This provides strong evidence that the main composition of the deposition layer covering the anode surface is SiO_2. Considering the porous microstructure of carbon deposition [6,12,17,44,45], a relatively dense silicon dioxide layer can be considered as the cause of blocking the fuel diffusion into the anode and causing the sudden failure.

Table 2
Results of XPS analysis showing amount of deposition species on the surface in % for OCV experiment.

Elements	Point 1	Point 2	Point 3	Complete failure
Si	2.53	23.66	28.98	30.37
C	55.37	34.8	16.83	10.21
O	31.46	40.35	54.08	59.24

3.3 Gas Chromatography for Exhuast Component Analysis

In order to verify the siloxane deposition mechanism on the Ni-YSZ anode, GC is also utilized for exhaust gas composition identification during the SOFC failure process. Besides H_2 and N_2, hydrocarbons and siloxanes can be detected in the exhaust as the compositions related to the products of the siloxane reaction on the anode. Due to the high concentration of siloxane (0.5%), several hydrocarbon components exist in the exhaust as the reaction products as shown in **Table 3**. From **Table 3**, the main gas phase product of siloxane deposition reaction is CH_4 and a relatively small amount of C_2H_6 and C_2H_4 were also observed. This result contradicts the previous siloxane mechanism shown in equation (1) which indicates CO should be the main component in exhaust gas besides H_2. No detectable level of CO was observed in the GC analysis results. The presence of a relatively high concentration of CH_4 also demonstrates the siloxane deposition mechanism is similar to the chemical adsorption process on the anode material surface like equation (3) and our previous studies suggest [25,30,34]. Specifically, the concentration of all hydrocarbons were below the GC calibration concentration after point 1. The highest concentration of CH_4 and other

hydrocarbons was detected after point 2 when the fast degradation process occurred. At point 3, when the SOFC is approaching complete failure, the methane concentration decreases.

Table 3
Results of the hydrocarbon compositions obtained from GC analysis of the SOFC exhaust during the OCV degradation experiments.

OCV	Methane (%)	Ethane (%)	Ethylene (%)
Point 1	<0.6	<0.04	<0.018
Point 2	1.16	<0.04	0.052
Point 3	0.73	<0.04	0.045
Uncertainty		± 2% measurement value	

In addition to the hydrocarbons, there are over 40 trace level species with detectable peaks in the GC spectra. The long retention time of those species in the spectra suggests they all belong to the heavy molecular weight compositions. Considering the inlet gas composition, there appears a high possibility that they also fall into the siloxane category. Due to the limitation of GC calibration, only 7 of the species having stronger signals can be identified as siloxane L2 to siloxane D5. In order to ensure there are no reactions before the D4 siloxane enters the SOFC, the GC results were also compared with the fuel mixture passing through the straight quartz tube reactor at ambient temperature and at 200 °C. Only 2.7% D4 loss has been detected when the D4 passes through the quartz tube indicating limited or no reactions occurring prior to the SOFC. In this case, all GC results for siloxane can be considered as products of the reactions occurring at high temperature in the reactor and SOFC. The unit of siloxane concentration is mg/m^3 due to the siloxane calibration method. From **Table 4**, unexpectedly, only a small amount of D4 can be found after passing through the high temperature SOFC/reactor compared with the inlet concentration at 0.5% (~38215 mg/m^3) and a much higher concentration of D3, L4, L5 appeared which means D4 is extremely active.

At point 1, linear structure siloxane L4 and L5 have been detected which may illustrate the ring-opening and polymerization process for D4 siloxane at the initial state of degradation. At point 2 when the failure event happened, GC results show the similar results to point 1. After point 3, L4 and L5 were replaced by D3 for the OCV experiment. More detailed explanation of the GC results will be discussed in the next part considering the electrochemical and morphology results.

Table 4
Results of the siloxane compositions from the GC analysis for the exhaust of OCV degradation experiments.

OCV	L2 (mg/m^3)	L3 (mg/m^3)	D3 (mg/m^3)	D4 (mg/m^3)	L4 (mg/m^3)	L5 (mg/m^3)	D5 (mg/m^3)	Total (mg/m^3)
Point 1	2.25	<0.3	2.12	4.99	69.40	32.81	<3.85	111.56
Point 2	1.99	<0.3	1.93	5.03	73.94	36.30	<3.85	121.41
Point 3	0.94	<0.3	73.00	14.92	1.33	3.21	<3.85	93.39
Uncertainty	± 10.2%	± 10.2%	± 10.2%	± 10.1%	± 10.2%	± 10.2%	± 10.1%	

3.4 Discussion

According to the morphology, XPS and electrochemical results analysis, the diffusion process obstruction by dense silicon dioxide deposition is primarily responsible for the failure of SOFC due to siloxane contamination. This conclusion contradicts the previous assumptions [29] that the blockage of the TPB causes the anode failure. Actually, the diffusion blockage failure has been implied by previous studies [22,23,25] which indicate the most severe siloxane deposition is located around the surface of the anode, typically far from the TPB. Following a failure mechanism investigation, a lifespan prediction of the SOFC can be attempted by connecting microstructure parameters to the essential event in the failure

process such as point 2 as the failure event. The microstructure parameters at failure event can also be utilized as a reference to recognize the cell conditions.

Three-dimensional Ni-YSZ microstructure and related geometric parameters have been investigated by focused ion beams (FIBs)-SEM technique for SOFC performance evaluation [46–48]. For the SOFC degradation studies, the FIB-SEM 3D reconstruction was utilized to have a trustworthy quantitative microstructure parameter analysis for electrode degradation including the tortuosity increase and the decrease of the porosity and the length of TPB [48,49]. For the SOFC anode degradation due to the intrinsic silicon contamination, the FIB-TEM technique was applied to the characterization of the SiO_2 segregation and accumulation at the anode/electrolyte interface and Ni/YSZ grain boundaries [50]. Recently, the in-situ, economical and non-destructive electrochemical method was proposed for the electrode's microstructure quantitative analysis. The electrochemical impedance spectra data was utilized for the ECM. Subsequently, the geometry parameters such as the tortuosity factor, length of TPB etc. can be calculated from the resistance values of the elements corresponding to the individual physicochemical process in ECM [39,40,51–53]. In this study, the electrochemical parameters obtained from the ECM can also be utilized for the anode microstructure characterization. The anode transmission line model in this study can also provide more microstructure information which can be applied as the reference for cell performance prediction and also reveal the anode degradation mechanism due to siloxane contamination.

Fuel diffusion through the porous Ni-YSZ anode can be simplified to a single Stefan-Maxwell diffusion mechanism governing process [53]. In this circumstance, the gas

diffusion polarization resistance can be theoretically given by equation (4) for the H_2-N_2 system.

$$R_W = \frac{\tau}{\varepsilon} \cdot \left(\frac{RT}{2F}\right)^2 \cdot \frac{L}{P} \cdot \frac{1}{D_{H_2,N_2}} \cdot \left[\frac{1}{\chi_{H_2}} + \frac{1}{\chi_{N_2}}\right] \quad (4)$$

The polarization resistance for ionic transport process can be also calculated by equation (5) [39,40].

$$r_{ion} = \frac{1}{\sigma_{ion,8YSZ}} \cdot \frac{\tau_{YSZ}}{\varepsilon_{YSZ}} \cdot \frac{1}{A_{act}} \quad (5)$$

The charge transfer polarization resistance for corresponding process at TPB can be obtained by equation (6).

$$r_{ct} = \frac{LSR_{ct}}{l_{TPB} \cdot A_{act}} \quad (6)$$

In equation (4), τ is the tortuosity factor for the fuel diffusion process in Ni-YSZ anode, ε is the porosity of entire Ni-YSZ anode, L is the diffusion length which can be considered as the thickness of the Ni-YSZ anode in this study because the anode is relatively thin. Atmospheric pressure was selected as the pressure of fuel in anode side which was denoted as P in the equations. χ_{H_2}, χ_{N_2} represent the mole fraction of the H_2 and N_2 in the fuel. D_{H_2,N_2} is the binary diffusion coefficient between the H_2 and N_2. The values of D_{H_2,N_2} was chosen as 2.10 cm^2s^{-1} [53].

For equation (5) as the ionic transport polarization resistance equation, $\sigma_{ion,8YSZ}$ is the theoretical oxygen ionic conductivity in 8YSZ. Similar to equation (4), τ_{YSZ} and ε_{YSZ} are tortuosity and porosity for the 8YSZ skeleton instead of the entire Ni-YSZ anode. The active electrode area of the anode is denoted by A_{act} in the equation.

The charge transfer polarization resistance can be calculated based on the equation (6). The LSR_{ct} is represented the line specific resistance of the triple phase boundary in the

Ni-YSZ anode and the value of LSR_{ct} can be obtained from the work accomplished by Utz et al. [54,55].

From the calculation based on previous equations, the ratio of porosity to tortuosity $\frac{\varepsilon}{\tau}$ can be obtained from the effective diffusion coefficient ($D_{theoretical} \cdot \frac{\varepsilon}{\tau}$) and effective oxygen ion conductivity ($\sigma_{theoretical} \cdot \frac{\varepsilon}{\tau}$) for the diffusion and ionic conduction polarization resistance. However, the porosity and tortuosity are both important geometric parameters for microstructure degradation investigation. Thus, the separation of these two parameters is necessary from the value of porosity to tortuosity ratio $\frac{\varepsilon}{\tau}$. Due to the fact that 3D microstructure reconstruction is not the purpose for this study, the rough 2D microstructure parameter investigation was conducted by morphology results for each point in the failure process. The porosity, as the relatively straightforward parameter to measure compared with the tortuosity, was acquired from the morphology results for the entire Ni-YSZ anode and YSZ skeleton. The porosity of each point has been presented in **table 5.**

Table 5
Results of the anode and YSZ skeleton porosity analysis for the OCV and 50 mA degradation experiments.

OCV	Porosity of entire Ni-YSZ anode (%)	Porosity of YSZ skeleton in the anode (%)
Point 1	14.4	26.6
Point 2	12.7	22.7
Point 3	7.3	21.4

50 mA cm^{-2}	Porosity of entire Ni-YSZ anode (%)	Porosity of YSZ skeleton in the anode (%)
Point 1	14.4	26.6
Point 2	7.4	24.1
Point 3	3.0	21.4

From the ionic transport polarization resistance equations (5), the tortuosity of YSZ anode skeleton τ_{YSZ}, can be calculated from the r_{ion} value and porosity. The τ_{YSZ} values for OCV and 50 mA cm^{-2} experiments are around 2.7 and 3.3, respectively, during the failure period. They are all reasonable values compared with the results from previous studies which are 1.9 from Dierickx et al. [39,40] and 4.5 to 6 reported by Nenning et al. [56]. From **Fig. 7**, with similar value throughout the experiments, both YSZ porosity and tortuosity for OCV and 50 mA cm^{-2} failure experiments did not have a significant change. This is likely due to the fact that the compact YSZ grains may be impenetrable for siloxane deposition. This result also reveals that the siloxane deposition does not have a significant influence on the oxygen ion conduction process in the anode.

The length of TPB of the Ni-YSZ anode can be obtained by equation (6). Shown in **Fig. 8**, due to the coverage of TPB by siloxane deposition, the decrease in the length of TPB can be detected. The values of the length of TPB before failure are 0.84 and 0.42 for OCV and 50 mA cm^{-2} experiments, respectively. They are much lower than the values reported by Dierickx et al. [39,40] which range from 1.61 to 2.061 for healthy fuel cells. However, in contrast to the sudden performance degradation of the SOFC after point 2, the TPB degradation process seems to be progressive. With a larger extent of TPB length decreasing, imposing polarization to the anode (under 50 mA cm^{-2}) can be considered as causing acceleration of the siloxane deposition process.

For the fuel diffusion process, which is related the eventually failure of the SOFC, the tortuosity of entire anode τ, can be calculated from the R_w value and porosity ε. The change of tortuosity and porosity value of the anode corresponds to the electrochemical and

morphology results satisfactorily (**Fig. 9**). Generally, the tortuosity decayed from around 2 to 6 for OCV and 50 mA cm^{-2} experiments. The tortuosity values before the total failure are much larger compared with normal values such as 3.034 from Dierickx et al. [39,40]; 1.36 suggested by Zhang et al. [53] and 1.42 to 1.56 reported by Zekri et al. [49]. For the OCV experiment, which had similar trends as the V-t Curve in **Fig. 2** and slow performance degradation occurring from point 1 to point 2, the tortuosity and porosity doesn't change significantly. After the initial failure event (point 2), the microstructure started to decay tremendously in which porosity decreased and tortuosity increased dramatically. For the 50 mA cm^{-2} experiment, also with the same general trends, the decay of microstructure was much faster than the SOFC in the OCV experiment with larger porosity drop. All of these results demonstrate that the failure of Ni-YSZ anode is highly dependent on the degradation of gas diffusion process. One thing deserves to draw attention is that the SOFC anode after the OCV and 50 mA cm^{-2} experiments have similar tortuosity values after point 3. It may demonstrate extremely serious coverage of the anode surface near the total blockage of the diffusion path. In this case, the two degraded anodes may share similar tortuosity.

As a summary, presenting those microstructure parameters and related electrochemical data during the SOFC failure process due to siloxane contamination can provide a useful reference for the anode lifetime prediction and also degradation mechanism investigation. However, even without accurate 3D reconstruction the microstructure parameters calculated in this section are complementary to other results in this study. The precise lifetime prediction for the anode under siloxane contamination still needs more experiments with different types of siloxanes and different concentrations in the future. Simultaneously, the

electrochemical and corresponding microstructure parameters acquired by 3D reconstruction techniques such as FIB-SEM should also be collected during the failure process.

After considering the electrochemical, morphology and exhaust gas composition analysis results comprehensively, a better understanding of the entire anode failure process due to siloxane emerges. Combining the electrochemical and morphology results presented from **Fig. 2** to **Fig. 6**, the faster SOFC anode degradation process starting around point 2 is because of the blockage of the fuel diffusion pathway in the anode. This conclusion can be supported by the much larger diffusion polarization resistance increase compared with other polarization processes in the whole failure process. The dense layer of SiO_2 on the anode surface from the morphology results also suggests severe obstruction of the diffusion process. Moreover, the microstructure calculation results from **Fig. 8** depict the incomplete invalidation of the TPB length, which follows a linearly decreasing trend instead of rapid degradation from point 2. This illustrates the TPB still remains active even with the failure of the SOFC.

To understand the siloxane deposition mechanism, valuable information was also provided by the exhaust gas composition analysis from GC. The high concentration of methane and absence of the CO in the exhaust suggests that the chemical adsorption mechanism (Eq. (3)) assumed in our previous studies is more acceptable than the siloxane reforming mechanism in equation (1) in which CO is one of the main products. Carbon deposition from the methane generated by the siloxane adsorption process can form a thin layer on the Ni particle [25] which can be proved both from the SEM/WDS and XPS results at point 1. The large amount of L4 and L5 siloxane present during the initial degradation of siloxane can provide strong evidence of the ring-opening reactions and the polymerization of

D4 siloxane into the anode. Cabrera-Codony et al. [57] also suggested that carbon surface can provide excellent sites for the adsorption and polymerization of cyclic siloxanes. In this case, the initial carbon deposition could accelerate the adsorption process further. Eventually, an amorphous silicon dioxide layer is formed upon the polymerized cyclic siloxanes layer [58]. From the GC results, the replacement of L4 and L5 by D3 may imply the end of the siloxane polymerization process and the starting of the silicon dioxide layer formation process. This step can also be verified by the fact that the appearance of the dense silicon dioxide layer in SEM/WDS (**Fig. 5** and **6**) occurs after the high concentration of D3 generation observed in GC results at point 3 in the OCV experiment. The large concentration of D3 instead of D4 during the silicon dioxide layer formation may be explained by the theoretical calculation from Vaiss et al. [58] that global silicon dioxide layer formation reactions from D4 compound are more stable than from D3. As a result, most of the D4 may directly deposit to silicon dioxide and part of D4 may be converted and remain as D3 due to higher stability of D3.

In this study, a faster failure process has been observed for the anode operating under polarization compared with the OCV condition. It can be confirmed from the following results for 50 mA cm^{-2} experiment:

(1) Reaching the failure event faster in the V-t curve.

(2) Larger performance loss and polarization resistance in electrochemical tests.

(3) Starting to form the silicon dioxide layer early from the SEM/WDS results.

(4) Worse microstructure parameters during the whole failure process based on calculations.

The faster silicon dioxide formation may result from direct electrochemical oxidation of the siloxane. In this study, the siloxane can directly encounter the active layer of the anode as the entire anode is only 17 μm thick. Considering the siloxane deposition mechanism discussed before, the faster silicon dioxide formation may also be explained by the quicker adsorption and establishment of the polymerized siloxane layer. The electrochemical reactions in the anode under polarization, such as equations (7) to (9) [59], can also offer different chemical groups for adsorption. These groups may accelerate the siloxane adsorption and polymerization process [30,34,58].

$$O_2 \rightleftharpoons 2O(ad) \quad (7)$$

$$H_2(g) + 2O(ad) \rightleftharpoons 2OH \quad (8)$$

$$H_2O(ad) \rightleftharpoons OH(ad) + H(ad) \quad (9)$$

Enlighten by the failure process investigation, the previous ppm(v) level siloxane contamination anode degradation studies in the literature were conducted during the gradual degradation process which consists of the siloxane adsorption, polymerization and starting of silicon dioxide formation process around point 1 to point 2 in this study. As a result, in order to reduce the siloxane deposition with ppm(v) level siloxane contamination in practical applications, these initial steps should be explored in the future. Blockage of the gas diffusion, which is considered as the main reason for the anode failure in this study, can also be relieved by special anode structure design such as separate anode supported and active layer with different porosity.

Conclusions

In order to investigate the failure process of the SOFCs' Ni-YSZ anode due to siloxane contamination, SOFCs were operated with D4 siloxane contaminating fuel under OCV and 50 mA cm^{-2} conditions at 800 °C. The sudden failure process of SOFCs can be observed after gradual degradation. The electrochemical characterization and morphology results indicate that the blockage of the fuel diffusion process in the anode is the key factor resulting in the rapid failure of the SOFCs. The GC and XPS results at the different stages of the failure process can also be provided valuable reference to further understand the siloxane deposition mechanism on the Ni-YSZ anode. The entire siloxane deposition processes including initial carbon deposition; siloxane polymerization and amorphous silicon dioxide deposition were proposed in this study based on morphology, XPS and GC results. Compared with the OCV experiment, the SOFCs operating under 50 mA cm^{-2} conditions experienced a faster failure process. This may be explained by the electrochemical processes in anode under polarization conditions can accelerate the siloxane adsorption and polymerization during the siloxane deposition.

Acknowledgement:

This material is based upon work supported by the U.S. Department of Energy under award number DE-EE0007721. We acknowledge the use of facilities within the Eyring Materials Center at Arizona State University supported in part by NNCI-ECCS-1542160.

Nomenclature

A_{act}:	Active area (cm^2)
AAL:	Anode active layer
ASL:	Anode support layer

CNLS:	Complex nonlinear least squares
D3:	Hexamethylcyclotrisiloxane
D4:	Octamethylcyclotetrasiloxane
D5:	Decamethylcyclopentasiloxane
D_{H_2,N_2}:	Binary diffusion coefficient between the H_2 and N_2 (cm^2s^{-1})
ECM:	Equivalent circuit model
EIS:	Electrochemical impedance spectroscopy
F:	Faraday's constant (C/mol)
FIB:	Focused ion beams
GC:	Gas chromatograph
L:	Diffusion length (μm)
L2:	Hexamethyldisiloxane
L3:	Octamethyltrisiloxane
L4:	Decamethyltetrasiloxane
L5:	Dodecamethylpentasiloxane
L_{TPB}:	Length of triple phase boundary (μm^{-2})
LSR:	Length specific resistance (Ω μm)
MFCs:	Mass flow controllers
OCV:	Open circuit condition
P:	Pressure of anode side gas (Pa)
Ppm (v):	Parts per million volume
R:	Universal gas constant ($J \cdot K^{-1} \cdot mol^{-1}$)
RMSE:	Residual root-mean-square error
R_W:	Gas diffusion resistance (Ω)
r_{ion}:	Ionic transport polarization resistance ($\Omega\ \mu m^{-1}$)
r_{ct}:	Charge transfer polarization resistance (Ω μm)
Sccm:	Standard cubic centimeters per minute
SEM:	Scanning electron microscope
SOFC:	Solid oxide fuel cell
T:	Temperature (°C)
TEM:	Transmission electron microscopy
TPB:	Triple phase boundary
WDS:	Wavelength-dispersive spectrometer
wt%:	Weight percentage
XPS:	Photoelectron spectroscopy
YSZ:	Yttria-stabilized zirconia
ε:	Porosity (%)
λ:	Regularization parameter
τ:	Tortuosity
σ:	Ionic conductivity ($S\ \mu m^{-1}$)
χ_{H2}:	Molar fraction of the H_2
χ_{N2}:	Molar fraction of the N_2

References:

[1] A. Weber, J. Szász, S. Dierickx, C. Endler-Schuck, E. Ivers-Tiffée, Accelerated Lifetime Tests for SOFCs, ECS Trans. 68 (2015) 1953–1960. https://doi.org/10.1149/06801.1953ecst.

[2] M. Heneka, E. Ivers-Tiffee, Accelerated Life Tests for Fuel Cells, ECS Meet. Abstr. MA2005-02 (2006) 1206–1206. https://doi.org/10.1149/MA2005-02/33/1206.

[3] W.Q. Meeker, L.A. Escobar, C.J. Lu, Accelerated Degradation Tests: Modeling and Analysis, Technometrics. 40 (1998) 89–99. https://doi.org/10.1080/00401706.1998.10485191.

[4] K. Sasaki, K. Haga, T. Yoshizumi, D. Minematsu, E. Yuki, R.-R. Liu, C. Uryu, T. Oshima, S. Taniguchi, Y. Shiratori, K. Ito, Impurity Poisoning of SOFCs, ECS Trans. 35 (2019) 2805–2814. https://doi.org/10.1149/1.3570280.

[5] Y. Kikuchi, J. Matsuda, Y. Tachikawa, Y. Shiratori, S. Taniguchi, K. Sasaki, Degradation of SOFCs by Various Impurities: Impedance Spectroscopy and Microstructural Analysis, ECS Trans. 78 (2017) 1253–1260. https://doi.org/10.1149/07801.1253ecst.

[6] M.S. Khan, S.B. Lee, R.H. Song, J.W. Lee, T.H. Lim, S.J. Park, Fundamental mechanisms involved in the degradation of nickel–yttria stabilized zirconia (Ni–YSZ) anode during solid oxide fuel cells operation: A review, Ceram. Int. 42 (2016) 35–48. https://doi.org/10.1016/j.ceramint.2015.09.006.

[7] M.B. Pomfret, J.C. Owrutsky, R.A. Walker, High-temperature raman spectroscopy of solid oxide fuel cell materials and processes, J. Phys. Chem. B. 110 (2006) 17305–17308. https://doi.org/10.1021/jp063952l.

[8] F.N. Cayan, M. Zhi, S.R. Pakalapati, I. Celik, N. Wu, R. Gemmen, Effects of coal syngas impurities on anodes of solid oxide fuel cells, J. Power Sources. 185 (2008) 595–602. https://doi.org/10.1016/j.jpowsour.2008.06.058.

[9] J.F.B. Rasmussen, A. Hagen, The effect of H_2S on the performance of Ni–YSZ anodes in solid oxide fuel cells, J. Power Sources. 191 (2009) 534–541. https://doi.org/10.1016/j.jpowsour.2009.02.001.

[10] D.-W. Choi, M. Ohashi, C.A. Lozano, J.W. Vanzee, P. Aungkavattana, S. Shimpalee, Sulfur diffusion of hydrogen sulfide contaminants to cathode in a micro-tubular solid oxide fuel cell, Electrochim. Acta. 321 (2019) 134713. https://doi.org/10.1016/j.electacta.2019.134713.

[11] A. Lussier, S. Sofie, J. Dvorak, Y.U. Idzerda, Mechanism for SOFC anode degradation from hydrogen sulfide exposure, Int. J. Hydrogen Energy. 33 (2008) 3945–3951. https://doi.org/10.1016/j.ijhydene.2007.11.033.

[12] B.B. Skabelund, H. Nakamura, T. Tezuka, K. Maruta, J. Ahn, R.J. Milcarek, Thermal partial oxidation of n-butane in a micro-flow reactor and solid oxide fuel cell stability assessment, Energy Convers. Manag. 254 (2022) 115222. https://doi.org/10.1016/j.enconman.2022.115222.

[13] V. Yurkiv, Reformate-operated SOFC anode performance and degradation considering solid carbon formation: A modeling and simulation study, Electrochim. Acta. 143 (2014) 114–128. https://doi.org/10.1016/j.electacta.2014.07.136.

[14] B. Stoeckl, V. Subotić, M. Preininger, H. Schroettner, C. Hochenauer, SOFC operation with carbon oxides: Experimental analysis of performance and degradation, Electrochim. Acta. 275 (2018) 256–264. https://doi.org/10.1016/j.electacta.2018.04.036.

[15] J. Kuhn, O. Kesler, Carbon deposition thresholds on nickel-based solid oxide fuel cell anodes II. Steam:carbon ratio and current density, J. Power Sources. 277 (2015) 455–463. https://doi.org/10.1016/j.jpowsour.2014.07.084.

[16] T.S. Li, W.G. Wang, T. Chen, H. Miao, C. Xu, Hydrogen sulfide poisoning in solid oxide fuel cells under accelerated testing conditions, J. Power Sources. 195 (2010) 7025–7032. https://doi.org/10.1016/j.jpowsour.2010.05.009.

[17] J.H. Koh, Y.S. Yoo, J.W. Park, H.C. Lim, Carbon deposition and cell performance of Ni-YSZ anode support SOFC with methane fuel, Solid State Ionics. 149 (2002) 157–166. https://doi.org/10.1016/S0167-2738(02)00243-6.

[18] A. Dhir, K. Kendall, Microtubular SOFC anode optimisation for direct use on methane, J. Power Sources. 181 (2008) 297–303. https://doi.org/10.1016/j.jpowsour.2007.11.005.

[19] D. Papurello, S. Silvestri, F. Biasioli, L. Lombardi, Wood ash biomethane upgrading system: A case study, Renew. Energy. 182 (2022) 702–712. https://doi.org/10.1016/j.renene.2021.10.037.

[20] G. Piechota, Removal of siloxanes from biogas upgraded to biomethane by Cryogenic Temperature Condensation System, J. Clean. Prod. 308 (2021) 127404. https://doi.org/10.1016/j.jclepro.2021.127404.

[21] D. Papurello, L. Tomasi, S. Silvestri, Proton transfer reaction mass spectrometry for the gas cleaning using commercial and waste-derived materials: Focus on the siloxane removal for SOFC applications, Int. J. Mass Spectrom. 430 (2018) 69–79. https://doi.org/10.1016/j.ijms.2018.05.002.

[22] H. Madi, A. Lanzini, S. Diethelm, D. Papurello, J. Van herle, M. Lualdi, J. Gutzon Larsen, M. Santarelli, Solid oxide fuel cell anode degradation by the effect of siloxanes, J. Power Sources. 279 (2015) 460–471. https://doi.org/10.1016/j.jpowsour.2015.01.053.

[23] H. Madi, S. Diethelm, S. Poitel, C. Ludwig, J. Van herle, Damage of Siloxanes on Ni-YSZ Anode Supported SOFC Operated on Hydrogen and Bio-Syngas, Fuel Cells. 15 (2015) 718–727. https://doi.org/10.1002/fuce.201400185.

[24] D. Papurello, A. Lanzini, SOFC single cells fed by biogas: Experimental tests with trace contaminants, Waste Manag. 72 (2018) 306–312. https://doi.org/10.1016/j.wasman.2017.11.030.

[25] J. Tian, R.J. Milcarek, Investigating the degradation mechanism of the solid oxide fuel cell nickel-yttria stabilized zirconia anode under siloxane contamination, J. Power Sources. 480 (2020) 229122. https://doi.org/10.1016/j.jpowsour.2020.229122.

[26] K. Haga, Y. Shiratori, K. Ito, K. Sasaki, Chemical Degradation and Poisoning Mechanism of Cermet Anodes in Solid Oxide Fuel Cells, ECS Trans. 25 (2019) 2031–2038. https://doi.org/10.1149/1.3205748.

[27] A. Chambers, I. Potter, Gas utilization from sewage waste, Carbon Energy Manag. Alberta Res. Counc. 1 (2002) 1–9. http://citeseerx.ist.psu.edu/viewdoc/download?doi=10.1.1.476.516&rep=rep1&type=pdf.

[28] D.M. Riley, J. Tian, G. Güngör-Demirci, P. Phelan, J.R. Villalobos, R.J. Milcarek, Techno-Economic Assessment of CHP Systems in Wastewater Treatment Plants, Environments. 7 (2020) 74. https://doi.org/10.3390/environments7100074.

[29] K. Haga, S. Adachi, Y. Shiratori, K. Itoh, K. Sasaki, Poisoning of SOFC anodes by various fuel impurities, Solid State Ionics. 179 (2008) 1427–1431. https://doi.org/10.1016/j.ssi.2008.02.062.

[30] J. Tian, R.J. Milcarek, Siloxane Deposition on the Ni-YSZ Solid Oxide Fuel Cell Anode Exposed to Bio-Syngas, J. Electrochem. Soc. 168 (2021) 044503. https://doi.org/10.1149/1945-7111/abf21a.

[31] N.H. Elsayed, A. Elwell, B. Joseph, J.N. Kuhn, Effect of silicon poisoning on catalytic dry reforming of simulated biogas, Appl. Catal. A Gen. 538 (2017) 157–164. https://doi.org/10.1016/j.apcata.2017.03.024.

[32] A.C. Sonoc, C. Thurgood, B. Peppley, D.G. Kelly, Kinetic study of the thermal decomposition of octamethylcyclotetrasiloxane on activated gamma alumina, J. Environ. Chem. Eng. 5 (2017) 4858–4865. https://doi.org/10.1016/j.jece.2017.07.057.

[33] C. Sun, R. Hui, J. Roller, Cathode materials for solid oxide fuel cells: a review, J. Solid State Electrochem. 14 (2010) 1125–1144. https://doi.org/10.1007/s10008-009-0932-0.

[34] J. Tian, R.J. Milcarek, Degradation Comparison of Cyclic and Linear Siloxane Contamination on Solid Oxide Fuel Cells Ni-YSZ Anode, Front. Energy Res. 9 (2021) 1–13. https://doi.org/10.3389/fenrg.2021.749771.

[35] C.M. Grgicak, R.G. Green, J.B. Giorgi, SOFC anodes for direct oxidation of hydrogen and methane fuels containing H2S, J. Power Sources. 179 (2008) 317–328. https://doi.org/10.1016/j.jpowsour.2007.12.082.

[36] L. Aguilar, S. Zha, Z. Cheng, J. Winnick, M. Liu, A solid oxide fuel cell operating on hydrogen sulfide (H_2S) and sulfur-containing fuels, J. Power Sources. 135 (2004) 17–24. https://doi.org/10.1016/j.jpowsour.2004.03.061.

[37] H.J. Ko, J.H. Myung, S.H. Hyun, J.S. Chung, Synthesis of LSM-YSZ-GDC dual composite SOFC cathodes for high-performance power-generation systems, J. Appl. Electrochem. 42 (2012) 209–215. https://doi.org/10.1007/s10800-012-0390-8.

[38] S. Masciandaro, M. Torrell, P. Leone, A. Tarancón, Three-dimensional printed yttria-stabilized zirconia self-supported electrolytes for solid oxide fuel cell applications, J. Eur. Ceram. Soc. 39 (2019) 9–16. https://doi.org/10.1016/j.jeurceramsoc.2017.11.033.

[39] S. Dierickx, J. Joos, A. Weber, E. Ivers-Tiffée, Advanced impedance modelling of Ni/8YSZ cermet anodes, Electrochim. Acta. 265 (2018) 736–750. https://doi.org/10.1016/j.electacta.2017.12.029.

[40] S. Dierickx, T. Mundloch, A. Weber, E. Ivers-Tiffée, Advanced impedance model for double-layered solid oxide fuel cell cermet anodes, J. Power Sources. 415 (2019) 69–82. https://doi.org/10.1016/j.jpowsour.2019.01.043.

[41] Sebastian, A. Weber, E. Ivers-Tiffée, How the distribution of relaxation times enhances complex equivalent circuit models for fuel cells, Electrochim. Acta. 355 (2020) 136764. https://doi.org/10.1016/j.electacta.2020.136764.

[42] V. Sonn, A. Leonide, E. Ivers-Tiffée, Combined Deconvolution and CNLS Fitting Approach Applied on the Impedance Response of Technical Ni/8YSZ Cermet Electrodes, J. Electrochem. Soc. 155 (2008) B675. https://doi.org/10.1149/1.2908860.

[43] X. Guo, R. Waser, Electrical properties of the grain boundaries of oxygen ion conductors: Acceptor-doped zirconia and ceria, Prog. Mater. Sci. 51 (2006) 151–210. https://doi.org/10.1016/j.pmatsci.2005.07.001.

[44] E. Rillo, M. Gandiglio, A. Lanzini, S. Bobba, M. Santarelli, G. Blengini, Life Cycle Assessment (LCA) of biogas-fed Solid Oxide Fuel Cell (SOFC) plant, Energy. 126 (2017) 585–602. https://doi.org/10.1016/j.energy.2017.03.041.

[45] M.A. Buccheri, J.M. Hill, Methane Electrochemical Oxidation Pathway over a Ni/YSZ and $La_{0.3}Sr_{0.7}TiO_3$ Bi-Layer SOFC Anode , J. Electrochem. Soc. 159 (2012) B361–B367. https://doi.org/10.1149/2.001204jes.

[46] J.R. Wilson, W. Kobsiriphat, R. Mendoza, H.Y. Chen, J.M. Hiller, D.J. Miller, K. Thornton, P.W. Voorhees, S.B. Adler, S.A. Barnett, Three-dimensional reconstruction of a solid-oxide fuel-cell anode, Nat. Mater. 5 (2006) 541–544. https://doi.org/10.1038/nmat1668.

[47] P.R. Shearing, J. Golbert, R.J. Chater, N.P. Brandon, 3D reconstruction of SOFC anodes using a focused ion beam lift-out technique, Chem. Eng. Sci. 64 (2009) 3928–3933. https://doi.org/10.1016/j.ces.2009.05.038.

[48] Z. Jiao, N. Shikazono, N. Kasagi, Quantitative Characterization of SOFC Nickel-YSZ Anode Microstructure Degradation Based on Focused-Ion-Beam 3D-Reconstruction Technique, J. Electrochem. Soc. 159 (2012) B285–B291. https://doi.org/10.1149/2.045203jes.

[49] A. Zekri, M. Knipper, J. Parisi, T. Plaggenborg, Microstructure degradation of Ni/CGO anodes for solid oxide fuel cells after long operation time using 3D reconstructions by FIB tomography, Phys. Chem. Chem. Phys. 19 (2017) 13767–13777. https://doi.org/10.1039/c7cp02186k.

[50] Y.L. Liu, C. Jiao, Microstructure degradation of an anode/electrolyte interface in SOFC studied by transmission electron microscopy, Solid State Ionics. 176 (2005) 435–442. https://doi.org/10.1016/j.ssi.2004.08.018.

[51] A. Kromp, A. Leonide, A. Weber, E. Ivers-Tiffée, Electrochemical Analysis of Reformate-Fuelled Anode Supported SOFC, J. Electrochem. Soc. 158 (2011) B980. https://doi.org/10.1149/1.3597177.

[52] A. Leonide, V. Sonn, A. Weber, E. Ivers-Tiffée, Evaluation and Modeling of the Cell Resistance in Anode-Supported Solid Oxide Fuel Cells, J. Electrochem. Soc. 155 (2008) B36. https://doi.org/10.1149/1.2801372.

[53] Y. Zhang, Y. Chen, F. Chen, In-situ quantification of solid oxide fuel cell electrode microstructure by electrochemical impedance spectroscopy, J. Power Sources. 277 (2015) 277–285. https://doi.org/10.1016/j.jpowsour.2014.11.123.

[54] A. Utz, K. V. Hansen, K. Norrman, E. Ivers-Tiffée, M. Mogensen, Impurity features in Ni-YSZ-H_2-H_2O electrodes, Solid State Ionics. 183 (2011) 60–70. https://doi.org/10.1016/j.ssi.2010.12.014.

[55] A. Utz, H. Störmer, A. Leonide, A. Weber, E. Ivers-Tiffée, Degradation and Relaxation Effects of Ni Patterned Anodes in H_2–H_2O Atmosphere, J. Electrochem. Soc. 157 (2010) B920. https://doi.org/10.1149/1.3383041.

[56] A. Nenning, M. Gerstl, M. Bram, A.K. Opitz, Mechanistic Insight into Porous Electrode Impedance: An Example of Ni+YSZ Cermet Anodes, ECS Trans. 91 (2019) 479–490. https://doi.org/10.1149/09101.0479ecst.

[57] A. Cabrera-Codony, M.A. Montes-Morán, M. Sánchez-Polo, M.J. Martín, R. Gonzalez-Olmos, Biogas upgrading: Optimal activated carbon properties for siloxane removal, Environ. Sci. Technol. 48 (2014) 7187–7195. https://doi.org/10.1021/es501274a.

[58] V.S. Vaiss, C.G. Fonseca, F.P.N. Antunes, L.S. Chinelatto Jr., S.S.X. Chiaro, W.F. Souza, A.A. Leitão, Experimental and Theoretical Study of Deactivated HDT Catalysts by Si Species Deposited on their Surfaces: Models Proposition, Structural and Thermodynamic Analysis, J. Catal. 389 (2020) 578–591. https://doi.org/10.1016/j.jcat.2020.06.007.

[59] K. Ong, J. Hanna, A.F. Ghoniem, Investigation of a Combined Hydrogen and Oxygen Spillover Mechanism for Syngas Electro-Oxidation on Ni/YSZ, J. Electrochem. Soc. 164 (2016) F32–F45. https://doi.org/10.1149/2.0161702jes.

Figures:

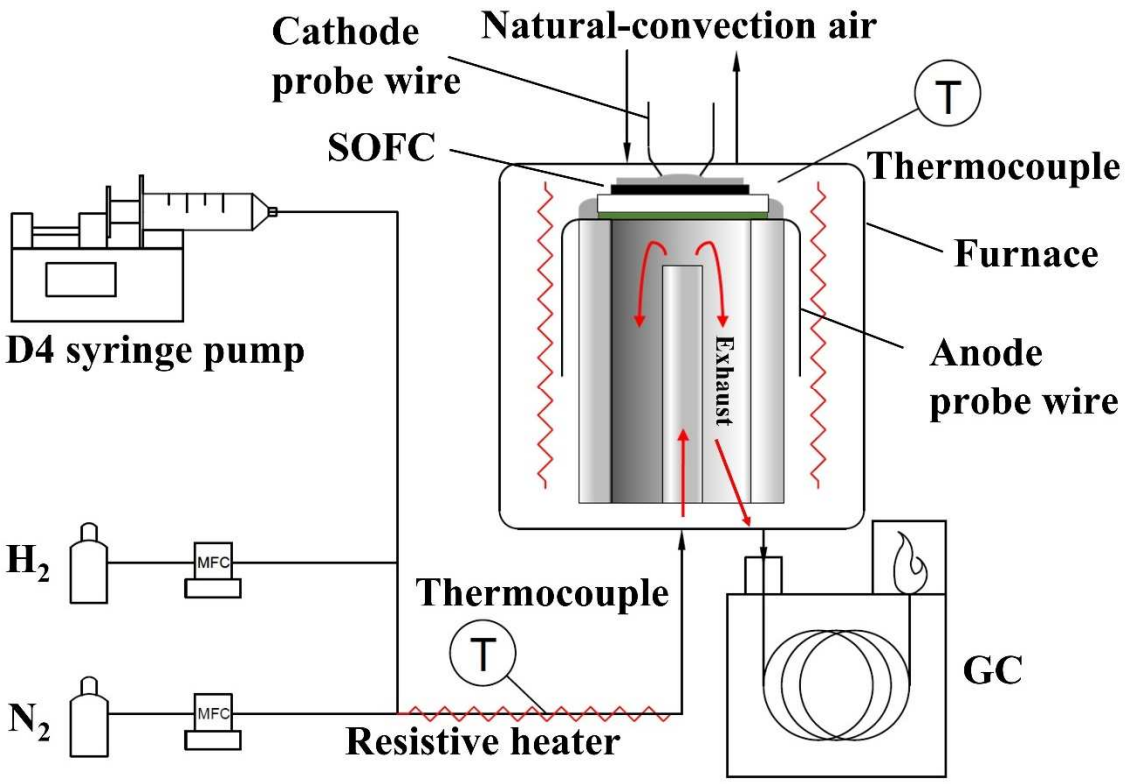

Fig 1. Schematic of the experiment setup.

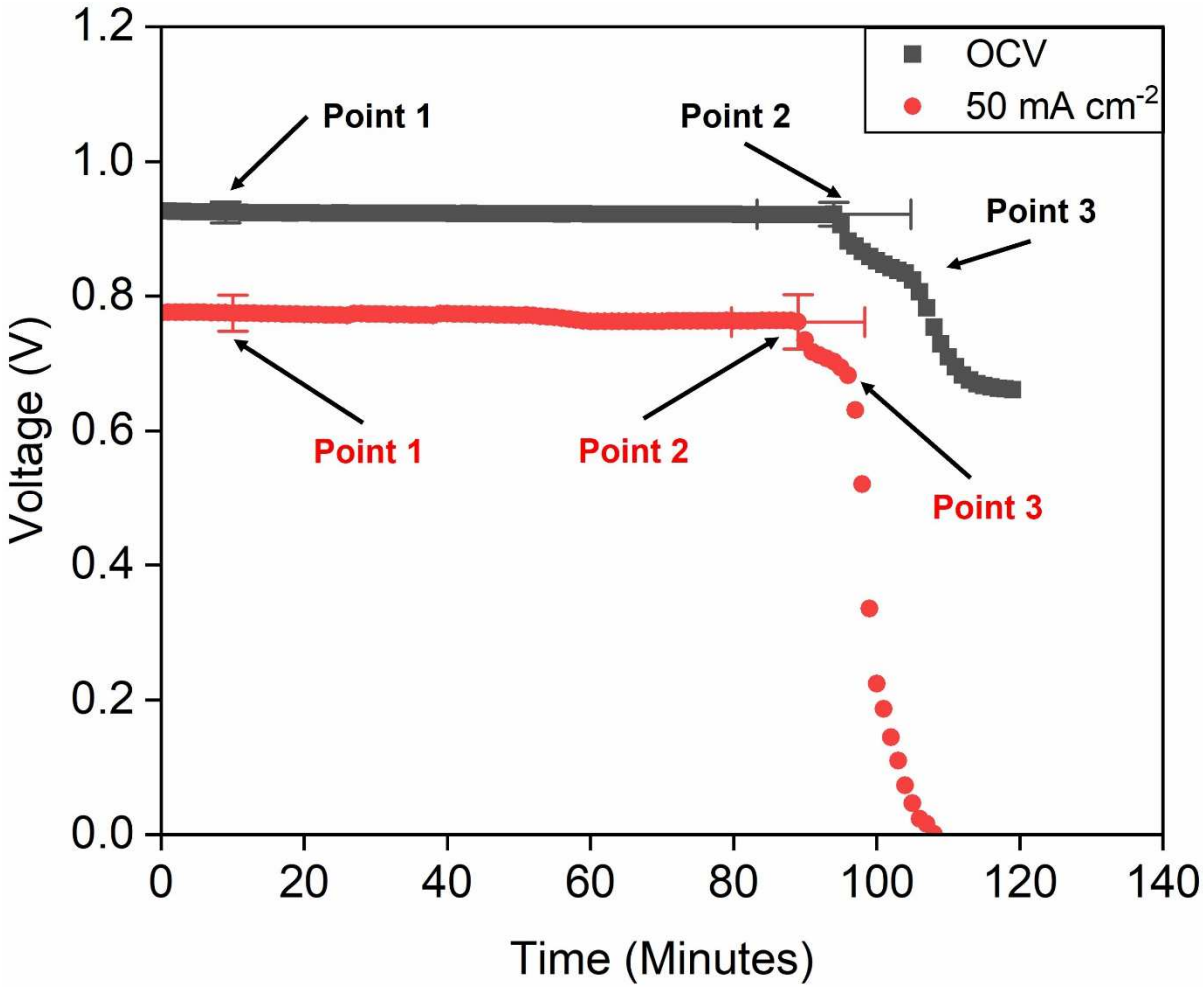

Fig 2. Voltage degradation of SOFCs under OCV and 50 mA cm^{-2} with 0.5% D4 siloxane contamination at 800 °C.

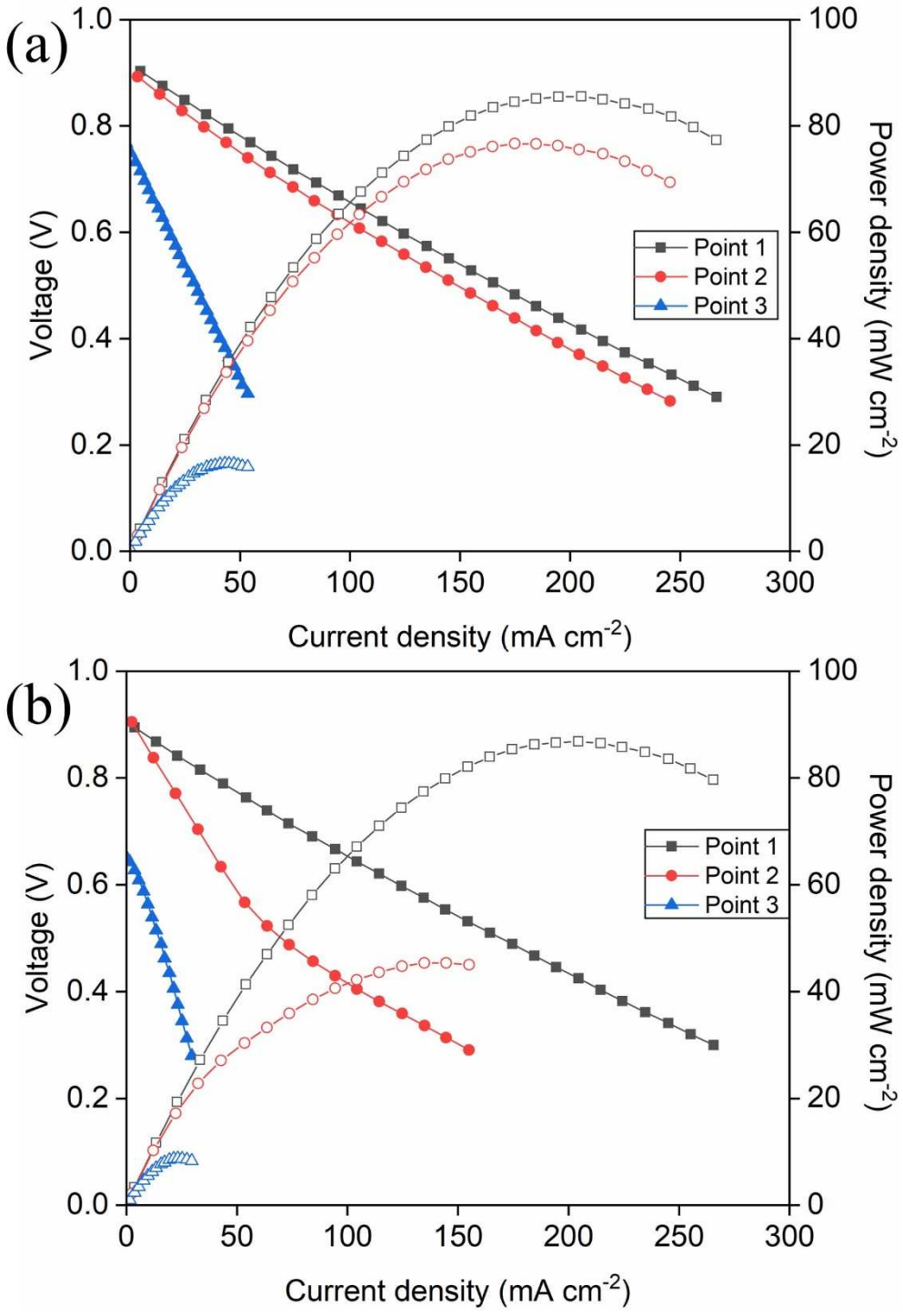

Fig. 3. Characterization of SOFC performance degradation by polarization curve (a) under OCV and (b) 50 mA cm^{-2} current density operation.

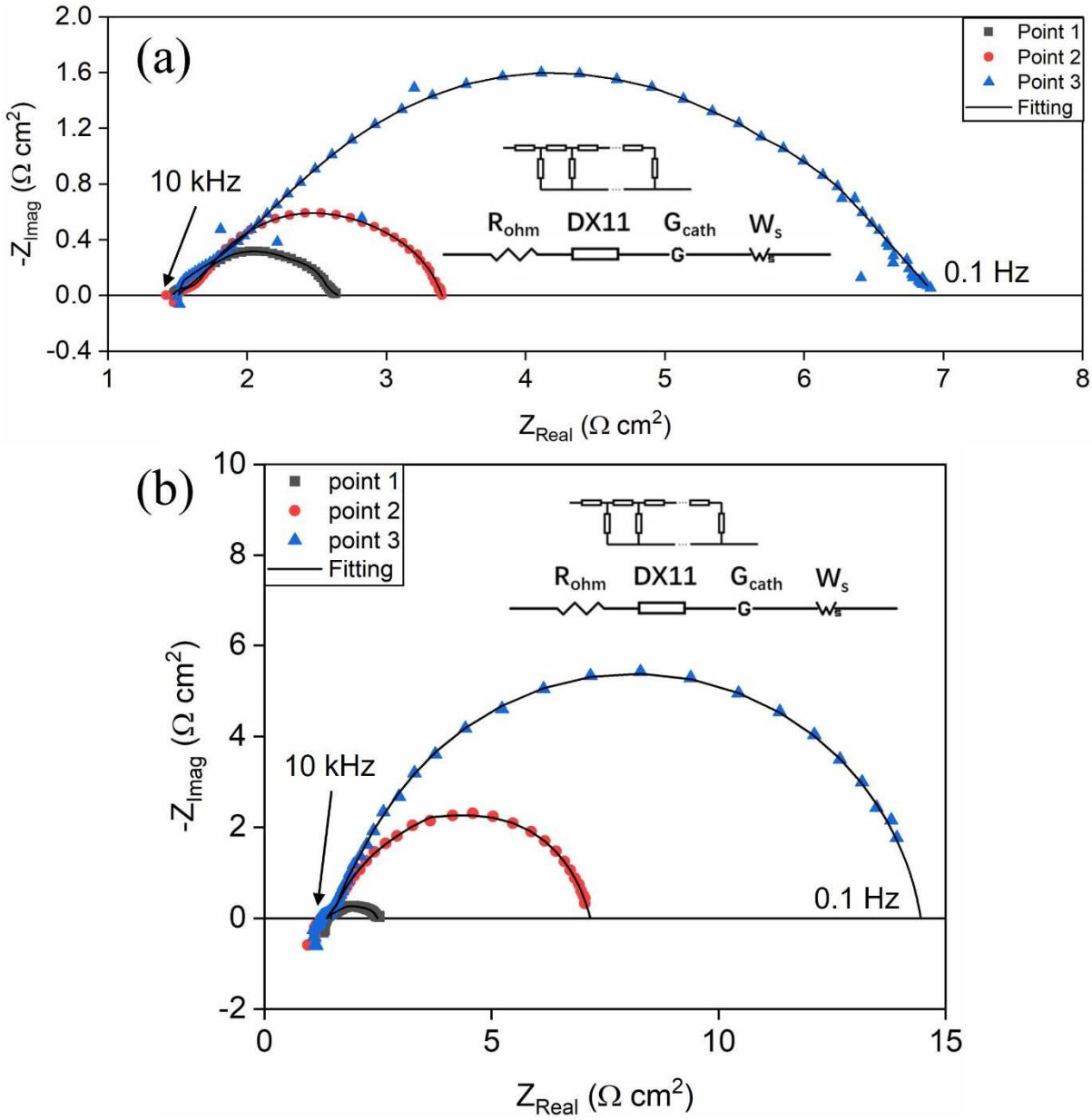

Fig. 4. Electrochemical analysis of the SOFC failure process by EIS and related equivalent circuit model (a) under OCV and (b) 50 mA cm^{-2} current density operation.

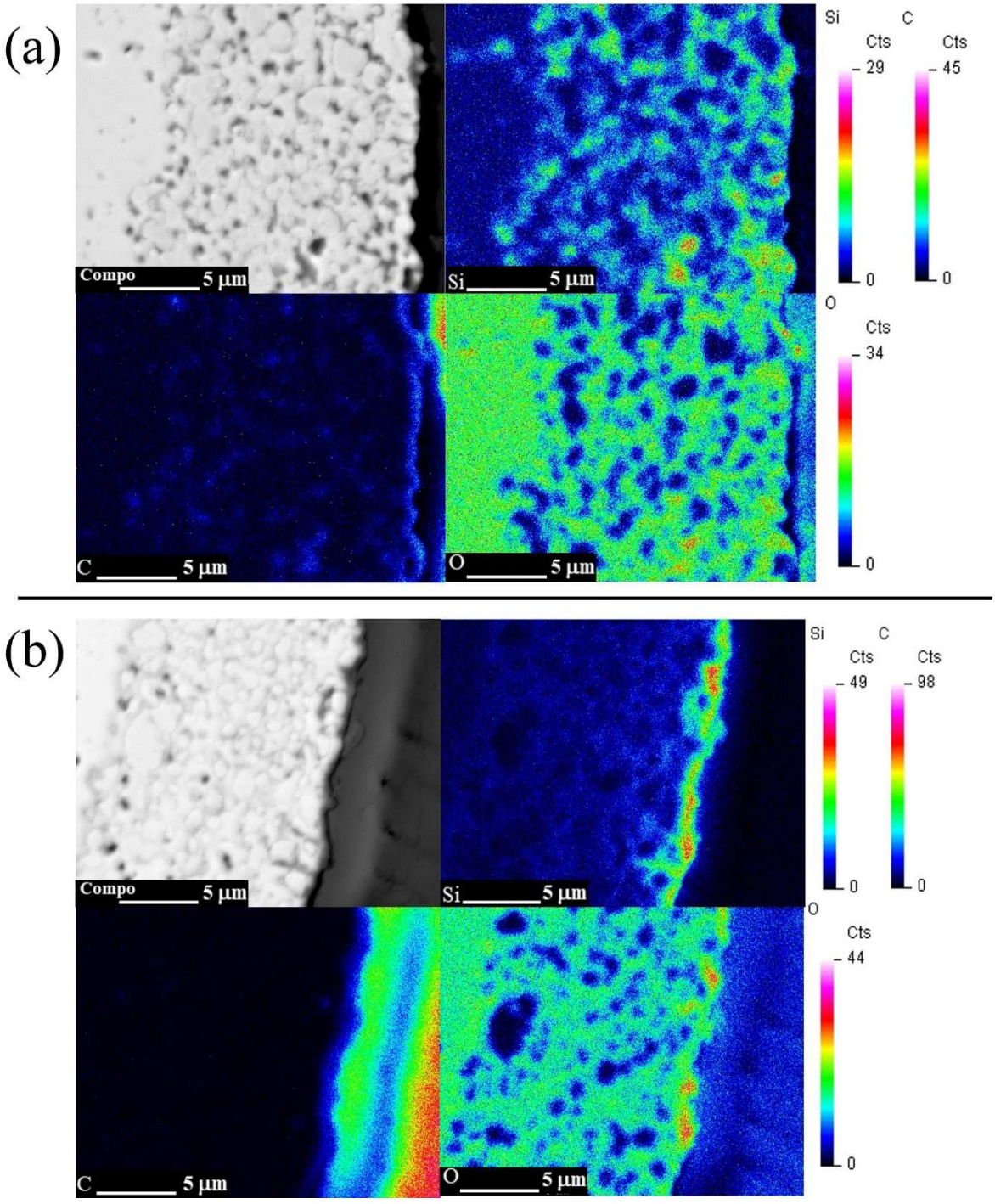

Fig. 5. SEM /WDS elemental mapping of the SOFC anode during the OCV experiment (a) after point 2 and (b) after point 3.

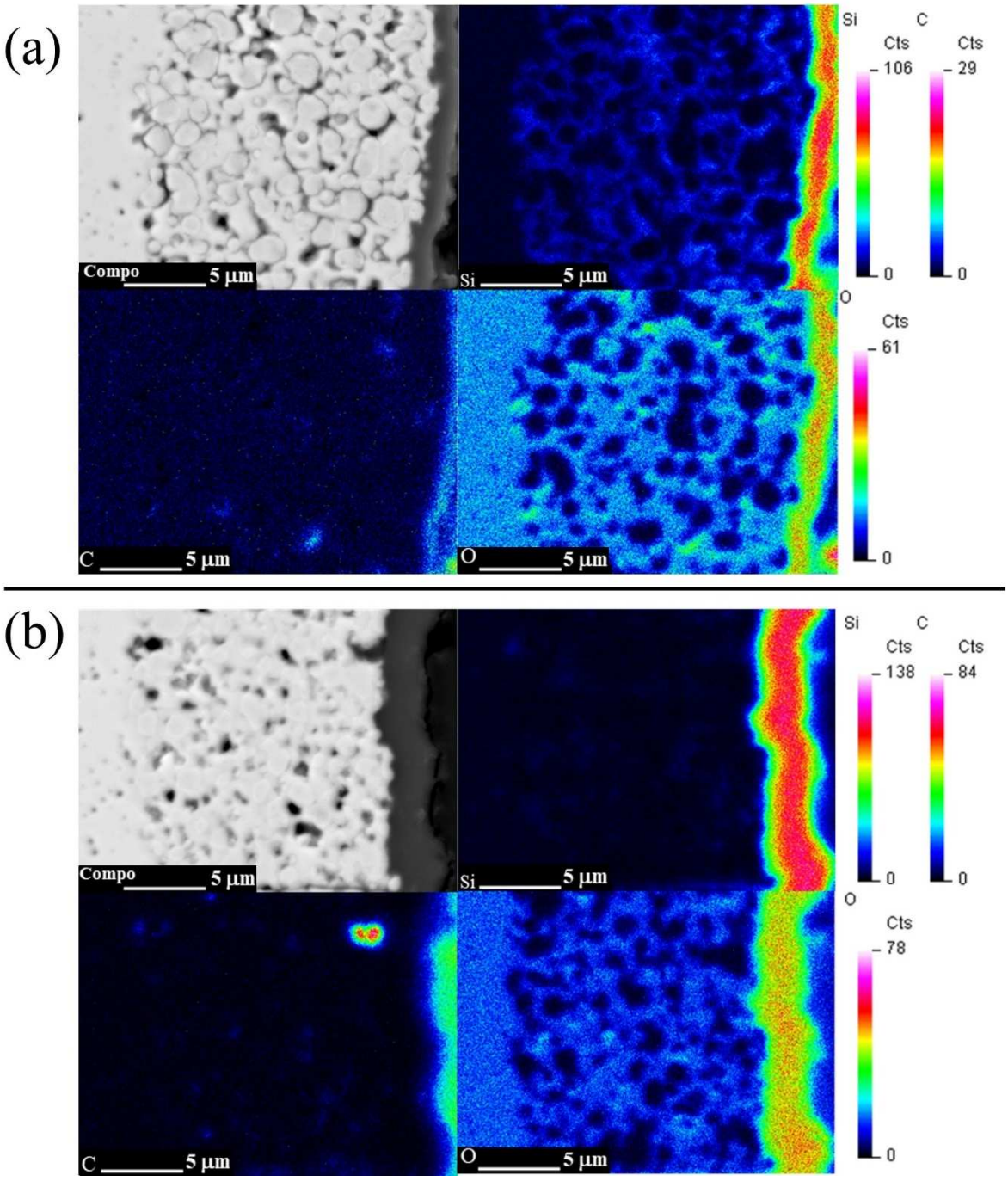

Fig. 6. SEM /WDS elemental mapping of the SOFC anode during the 50 mA cm^{-2} current density experiment (a) after point 2 and (b) after point 3.

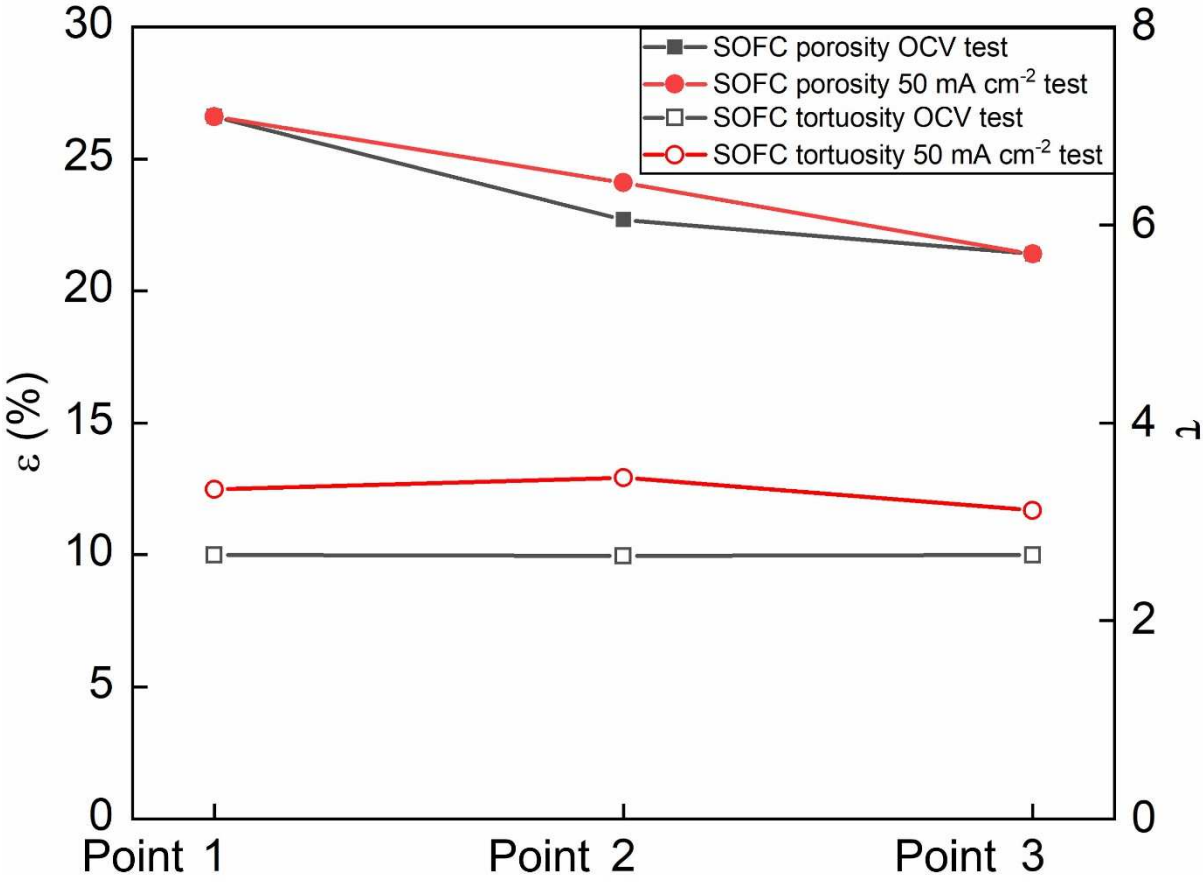

Fig. 7. The porosity and corresponding tortuosity change of the YSZ anode skeleton during OCV and 50 mA cm^{-2} D4 contamination experiments.

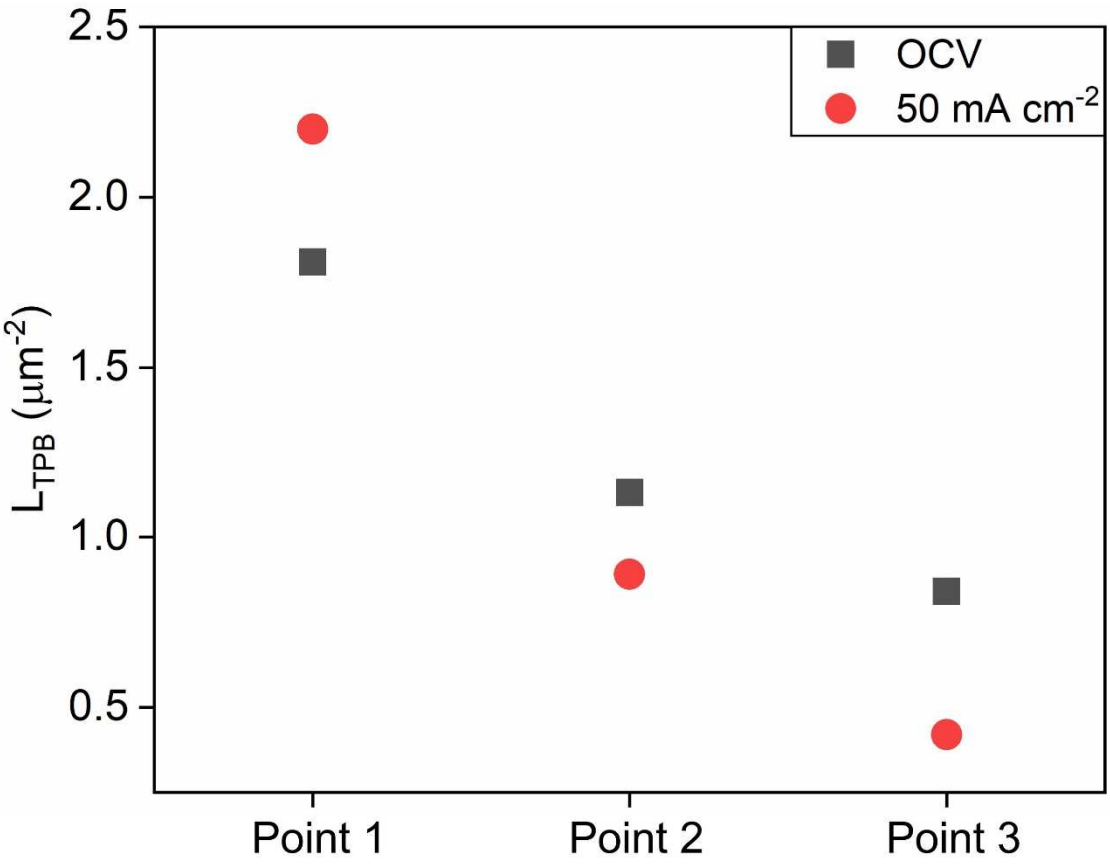

Fig. 8. The length of triple phase boundary change of the Ni-YSZ anode during OCV and 50 mA cm^{-2} D4 contamination experiments.

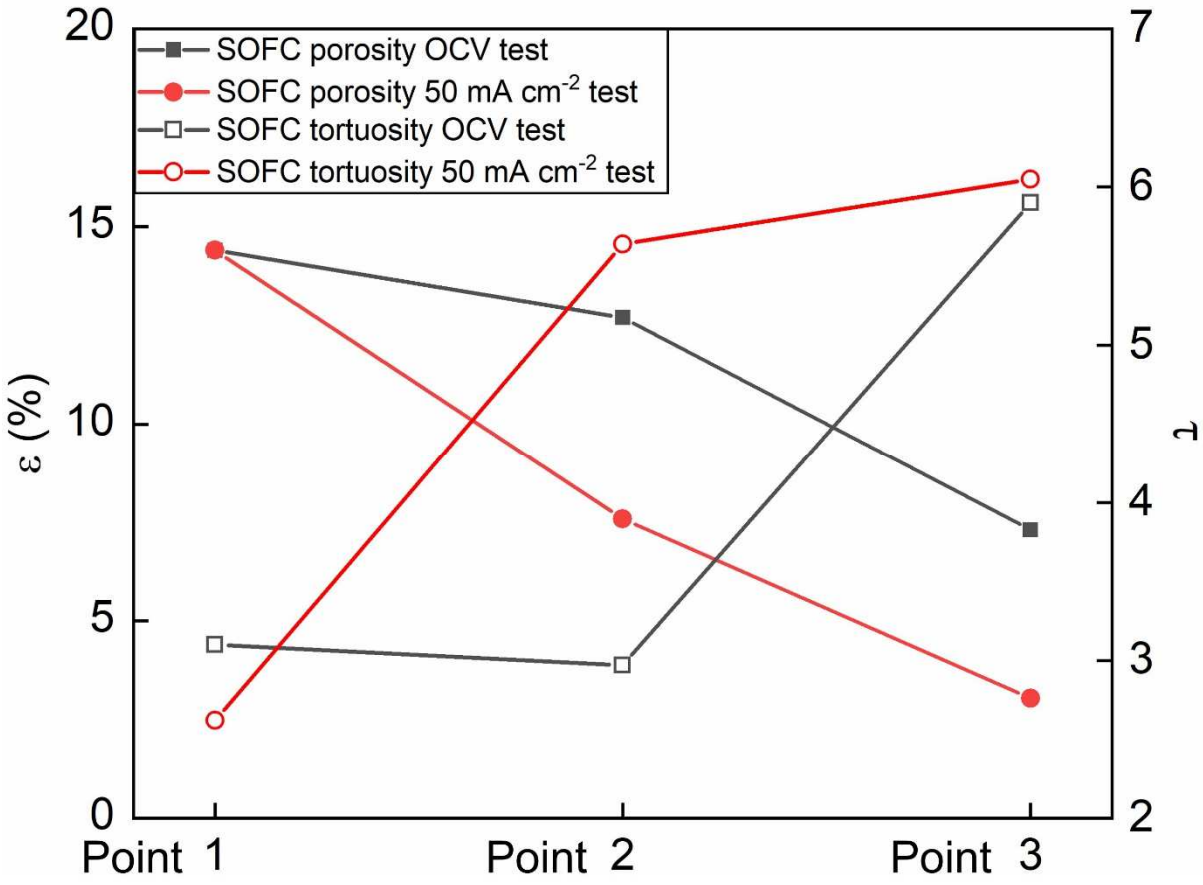

Fig. 9. The porosity and corresponding tortuosity change of the entire anode during OCV and 50 mA cm^{-2} D4 contamination experiments.

Figures Captions:

Fig 1. Schematic of the experiment setup.

Fig 2. Voltage degradation of SOFCs under OCV and 50 mA cm^{-2} with 0.5% D4 siloxane contamination at 800 °C.

Fig. 3. Characterization of SOFC performance degradation by polarization curve (a) under OCV and (b) 50 mA cm^{-2} current density operation.

Fig. 4. Electrochemical analysis of the SOFC failure process by EIS and related equivalent circuit model (a) under OCV and (b) 50 mA cm^{-2} current density operation.

Fig. 5. SEM /WDS elemental mapping of the SOFC anode during the OCV experiment (a) after point 2 and (b) after point 3.

Fig. 6. SEM /WDS elemental mapping of the SOFC anode during the 50 mA cm^{-2} current density experiment (a) after point 2 and (b) after point 3.

Fig. 7. The porosity and corresponding tortuosity change of the YSZ anode skeleton during OCV and 50 mA cm^{-2} D4 contamination experiments.

Fig. 8. The length of triple phase boundary change of the Ni-YSZ anode during OCV and 50 mA cm^{-2} D4 contamination experiments.

Fig. 9. The porosity and corresponding tortuosity change of the entire anode during OCV and 50 mA cm^{-2} D4 contamination experiments.

Graphical Abstract